An ERT-based Robotic Skin with Sparsely Distributed Electrodes: Structure, Fabrication, and DNN-based Signal Processing

Kyungseo Park, *Student Member, IEEE*, Hyunkyu Park, *Student Member, IEEE*,
Hyosang Lee, *Member, IEEE*, Sungbin Park, *Student Member, IEEE*, *Jung Kim, *Member, IEEE*

Abstract— Electrical resistance tomography (ERT) has previously been utilized to develop a large-scale tactile sensor because this approach enables the estimation of the conductivity distribution among the electrodes based on a known physical model. Such a sensor made with a stretchable material can conform to a curved surface. However, this sensor cannot fully cover a cylindrical surface because in such a configuration, the edges of the sensor must meet each other. The electrode configuration becomes irregular in this edge region, which may degrade the sensor performance. In this paper, we introduce an ERT-based robotic skin with evenly and sparsely distributed electrodes. For implementation, we sprayed a carbon nanotube (CNT)-dispersed solution to form a conductive sensing domain on a cylindrical surface. The electrodes were firmly embedded in the surface so that the wires were not exposed to the outside. The sensor output images were estimated using a deep neural network (DNN), which was trained with noisy simulation data. An indentation experiment revealed that the localization error of the sensor was 5.2 ± 3.3 mm, which is remarkable performance with only 30 electrodes. A frame rate of up to 120 Hz could be achieved with a sensing domain area of 90 cm^2. The proposed approach simplifies the fabrication of 3D-shaped sensors, allowing them to be easily applied to existing robot arms in a seamless and robust manner.

I. INTRODUCTION

In an unstructured environment, robots interacting with people must obtain information about their surroundings because such information is directly related to decision making, motion planning, and human safety [1], [2]. Audiovisual data can be utilized to recognize the external environment, but it is difficult to obtain data about physical contact from a camera or microphone. Thus, a robot needs another complementary sensory system for measuring physical interaction. Furthermore, such physical contact data can be combined with visual data to allow robots to perform contact-rich tasks [3].

Since physical contacts can occur on any part of a robot, there is a need to develop a whole-body robotic skin. Tactile sensors have been studied for use in robotic skin, but most of them are limited to small-scale applications, such as fingertip sensors. It is not easy to extend these works to a larger scale because the electrical wiring becomes highly complex as the number of sensing points increases. This is a major obstacle
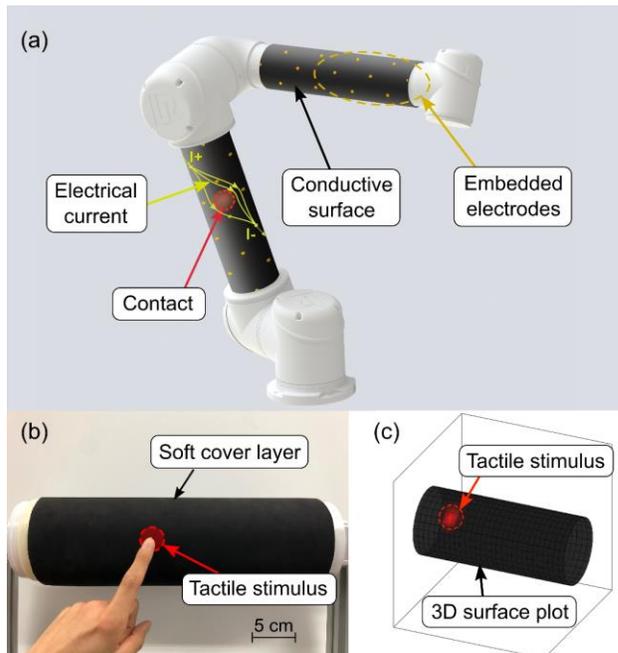

Figure 1. (a) Concept of an ERT-based 3D robotic skin with distributed and embedded electrodes; (b) the completed tactile sensor; (c) image reconstruction result on a 3D surface plot

for large-scale tactile sensors. Nevertheless, several methods have been introduced to address this wiring issue.

Array indexing utilizes orthogonally aligned electrodes to measure physical quantities at the intersections of the electrodes. This approach can efficiently reduce the number of electrodes needed by accessing sensing points through combinations of electrodes [4]. However, all sensing points related to an electrode become unavailable when that electrode fails, and it is also not easy to repair such a sensor. In the modularization approach, physical quantities such as voltage and capacitance are measured by individual sensor modules [5]–[7]. The measured data are transferred through serial communication, so only a few channels are required. However, each module has its own micro control unit (MCU); consequently, the energy consumption increases as the number of modules increases. In addition, these modularized sensors are based on flexible PCBs, which have difficulty covering a complexly curved surface.

K. Park, H. Park, S. Park, and J. Kim are with Korea Advanced Institute of Science and Technology, Daejeon 34141, South Korea. (e-mail: bbq2686, hkpark94, robot0826, jungkim@kaist.ac.kr)

H. Lee is with the Max Planck Institute for Intelligent Systems, Stuttgart, 70569 Germany. (e-mail: hslee@is.mpg.de)

In contrast, electrical resistance tomography (ERT) has been introduced to implement large and curved soft tactile sensors due to its unique working principle [8]. ERT is a virtual sensing technique in which the conductivity distribution of an inner sensing domain is estimated using only several boundary electrodes. This is a remarkable advantage for a large-scale tactile sensor because the sensing points and electrodes are untethered to each other. As a result, the shape of the sensor and the electrode configuration can be freely customized depending on the application requirements. Previously, we introduced an ERT-based tactile sensor made with a conductive fabric [9]. Since the developed sensor was stretchable and durable, it showed promising results, such as scalability, conformability, and ease of fabrication. However, the electrical wires were exposed to the outside, and modeling error arose during attachment. It was also challenging to cover a cylindrical surface.

In this paper, we introduce an ERT-based robotic skin with sparsely distributed electrodes to achieve a tactile sensing capability on a cylindrical surface. The concept of the developed robotic skin is shown in **Fig. 1**. The electrodes are evenly and sparsely distributed over the surface and are firmly embedded in the robotic skin. The conductive domain is formed by spraying a carbon nanotube (CNT)-dispersed solution on the cylindrical surface. To form a piezoresistive structure, we also cover the rigid part with an array of highly conductive fabric patches. When the sensor is indented, a contact resistance is formed between the coating layer and the fabric patches, causing the conductivity to locally decrease. The output signal is processed by a deep neural network (DNN) that has been trained on noisy simulation data.

This paper is organized as follows: Section II briefly explains the working principle and procedure of ERT, along with some mathematical formulations. Then, the neural-network-based image reconstruction technique is explained. The sensor structure and fabrication process are described in Section III. Next, the performance of the sensor is investigated in Section IV by means of an indentation experiment. Finally, the results of this research are discussed in Section V.

II. Electrical resistance tomography

ERT is a geophysical technique for imaging the subsurface structure of the ground [10]–[13]. It is closely related to electrical impedance tomography (EIT), which is used for medical imaging [14]–[17] and in industrial applications [18]–[21]. The major advantage of ERT is that the conductivity distribution of the sensing domain can be mathematically reconstructed using boundary voltages because it is known, based on a physical model, how the boundary voltages are determined from the conductivity distribution. The ERT procedure consists of two parts: one is a forward problem, and the other is an inverse problem. The forward problem is to simulate the electrical behavior of the sensor by solving a partial differential equation with given conditions such as the base conductivity, the shape of the domain, and the boundary conditions. The inverse problem is to reconstruct the conductivity image from the boundary voltages. This procedure can be numerically implemented by means of EIDORS, which is an open-source MATLAB library for EIT [22], [23]. This software suite includes the functions for the mesh generation, drive pattern, forward solving, image reconstruction, etc. The details are described in the following section, along with mathematical formulations.

A. Forward problem

For a conductive domain Ω and its boundary $\partial\Omega$, the ERT forward problem is to find the boundary potential ϕ on $\partial\Omega$ due to the given conductivity σ. Maxwell's equations give the following relationship between the boundary potential ϕ and the conductivity distribution σ in the region Ω under the assumption of direct current and the absence of any interior current source:

$$\nabla \cdot (\sigma \nabla \phi) = 0 \quad \text{in } \Omega \tag{1}$$

If the conductivity is known, the potential can be estimated from knowledge of the boundary conditions on $\partial\Omega$:

$$j = \sigma \nabla \phi \cdot \mathbf{n} \quad \text{on } \partial\Omega \tag{2}$$

where j is the current density and $\mathbf{n}$ denotes the outward unit vector normal to $\partial\Omega$. This is a Dirichlet–Neumann boundary value problem for the Laplacian elliptical partial difference equation expressed in (1). To solve this equation, we first need to build a forward model for the finite element method (FEM); this model is composed of nodes connected to adjacent nodes and can be regarded as a passive resistor network that is equivalent to the sensor. Then, the electrical behavior of the conductive domain is described by a transfer impedance matrix $\mathbf{R}(\sigma) \in \mathbb{R}^{N \times N}$ such that

$$\mathbf{v}(\cdot \, ; \sigma, \mathbf{i}) = \mathbf{R}(\sigma) \, \mathbf{i} \tag{3}$$

where $\mathbf{i} \in \mathbb{R}^N$ and $\mathbf{v} \in \mathbb{R}^N$ are the current through a finite element and the resulting potential across it, respectively [24]. The transfer impedance matrix $\mathbf{R}(\sigma)$ is determined by the conductivity distribution σ in the conductive domain Ω. Current can only be injected through the nodes corresponding to the electrodes, so we can reduce the network by neglecting the other nodes, as shown below:

$$\hat{\mathbf{v}}(\cdot \, ; \sigma, \mathbf{p}) = \mathbf{S}(\sigma) \, \mathbf{p} \tag{4}$$

where $\mathbf{p} \in \mathbb{R}^L$ is the current vector injected into the electrodes and $\hat{\mathbf{v}} \in \mathbb{R}^L$ represents the resulting voltages on the electrodes. The real symmetric matrix $\mathbf{S}(\sigma) \in \mathbb{R}^{L \times L}$ is the transfer impedance matrix of the reduced network with respect to only the L nodes corresponding to electrodes. For the conductivity change $\Delta\sigma$, the change in the measurement voltages Δe for measurement pattern $\mathbf{m} \in \mathbb{R}^{L \times 1}$ and injection pattern $\mathbf{p} \in \mathbb{R}^{L \times 1}$ can be determined as shown below:

$$\Delta e = \mathbf{m}^{\mathbf{T}} \{ \hat{\mathbf{v}}(\cdot \, ; \sigma + \Delta\sigma, \mathbf{p}) - \hat{\mathbf{v}}(\cdot \, ; \sigma, \mathbf{p}) \}$$
$$= \mathbf{m}^{\mathbf{T}} \big(\mathbf{S}(\sigma + \Delta\sigma) - \mathbf{S}(\sigma) \big) \mathbf{p} \tag{5}$$

By means of the transfer impedance matrix, the electrical behavior of the sensor can be described by a linear equation. The injection and measurement vectors $\mathbf{p}$ and $\mathbf{m}$ can be extended to matrix form as shown below:

$$\Delta \mathbf{E} = \mathbf{M^T}(\Delta \mathbf{S})\mathbf{P} \qquad (6)$$

where $\mathbf{P} = [\mathbf{p}_1, \mathbf{p}_2, \cdots \mathbf{p}_n]$ and $\mathbf{M} = [\mathbf{m}_1, \mathbf{m}_2, \cdots, \mathbf{m}_m]$. Then, the resulting measurement $\Delta \mathbf{E} \in \mathbb{R}^{m \times n}$ is expressed in vectorized form with a Kronecker product as follows:

$$\Delta \mathbf{E}_{vec} = (\mathbf{P^T} \otimes \mathbf{M^T})\Delta \mathbf{S}_{vec} = \mathbf{G}\,\Delta \mathbf{S}_{vec} = \mathbf{J}\,\Delta \sigma \qquad (7)$$

where $\Delta \mathbf{S}_{vec}$ denotes the vectorization of the transfer impedance matrix $\Delta \mathbf{S}$. The matrix $\mathbf{G} \in \mathbb{R}^{mn \times L^2}$ is defined to express the relationship between the vector $\Delta \mathbf{S}_{vec}$ and the resulting voltages $\Delta \mathbf{E}_{vec}$ for the given pattern matrices. Here, the Jacobian matrix $\mathbf{J}$ can be said to represent the relationship between the conductivity change $\Delta \sigma$ and $\Delta \mathbf{E}_{vec}$.

B. Inverse problem

The goal of the ERT inverse problem is to estimate the conductivity distribution σ from the measured voltage. However, this is an ill-posed and nonlinear problem. Consequently, linearization and regularization are applied to solve the EIT inverse problem. First, the nonlinear relationship between the conductivity σ and the measured potential $\mathbf{E}$ needs to be approximated by the linear equation below:

$$\Delta \mathbf{E}_{vec} = \mathbf{J}\,\Delta \sigma + \mathbf{w} \qquad (8)$$

where $\mathbf{J}$ is the Jacobian matrix and $\mathbf{w}$ is the measurement noise. Then, the linearized inverse problem can be solved by calculating the pseudoinverse of the Jacobian matrix $\mathbf{J}$. However, this calculation is difficult for a fine mesh because the rank of $\mathbf{J}$ is smaller than the number of mesh elements. Therefore, we need to introduce additional *a priori* information to supplement the available data. Then, the linearized inverse problem can be solved by minimizing the cost function shown below:

$$\lambda(\Delta \sigma) = \|\delta \mathbf{E} - \mathbf{J}\Delta \sigma\|_2^2 + \|\alpha\,\mathbf{\Gamma}\Delta \sigma\|_2^2 \qquad (9)$$

where $\mathbf{\Gamma} \in \mathbb{R}^{M \times M}$ is a regularization matrix established based on *a priori* knowledge, such as a spatial high-pass filter or NOSER [25]. The level of regularization is adjusted by the hyperparameter α. Finally, the relationship between $\Delta \sigma$ and $\delta \mathbf{E}$ is approximated as follows:

$$\Delta \tilde{\sigma} = (\mathbf{J^T J} + \alpha^2 \mathbf{\Gamma^T \Gamma})^{-1} \mathbf{J^T}\,\delta \mathbf{E} = \mathbf{Q}\,\delta \mathbf{E} \qquad (10)$$

where $\mathbf{Q}$ is the regularized linear reconstruction matrix. By using this approximate equation, the reconstructed image can be analytically stabilized.

C. DNN-based image reconstruction

Even if we obtain a stable output image by approximating the inverse problem, the output image is still blurred and distorted due to the regularization and linearization. For more accurate reconstruction, an iterative reconstruction method can be adopted [14], [26], but this will incur a high computational cost. Considering the importance of the sampling frequency, the iterative approach is not practical for robotic skin applications. Thus, it is desirable to develop a reconstruction method for the ERT inverse problem that is not only accurate but also fast. Neural networks have shown promising results for addressing the nonlinearity of the ERT
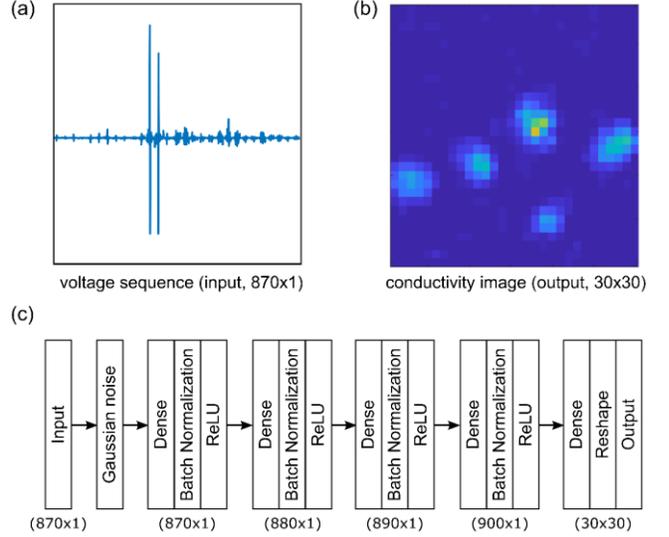

Figure 2. DNN for ERT image reconstruction: (a) example of an input voltage sequence; (b) example of a conductivity image with perturbations; (c) scheme of the network

inverse problem with a suitable computational speed [27]–[30]. Park et al. proposed a DNN approach for an EIT-based real-time soft tactile sensor [31]. The results revealed that the blurring effect of the sensor was successfully mitigated by means of the DNN, while the frame rate of the sensor was still fast compared to the iterative approach [26]. Thus, we utilize a similar network architecture in this paper.

The scheme of the network is shown in **Fig. 2**. The neural network is designed with four fully connected layers. The numbers of neurons in each hidden layer, from first to last, are empirically selected as 870, 880, 890, and 900. The input variables in each hidden layer are modified by batch normalization, and the activation function is the rectified linear unit (ReLU) function. Training data were obtained by solving the forward problem for a 3D ERT model. In each simulation, Gaussian-shaped conductivity perturbations were applied at several locations on the sensor, as shown in **Fig. 2(b)**. The conductivity image was defined on an automatically generated mesh, which was mapped to a 30-by-30 rectangular grid for visibility.

The perturbed conductivity image was used as an output variable for the training dataset. The simulated voltages were also obtained from the given conductivity perturbations and electrode pattern. We used an adjacent pattern such that the length of the voltage vector was 870. The simulated voltages were normalized with respect to their mean and standard deviation and used as an input variable for the training dataset. The total number of samples in the training dataset was approximately 1,100,000. A test dataset was also generated through simulations with randomly perturbed conductivity images. The number of samples in the test dataset was 40,000, and the test dataset was also normalized with respect to the mean and standard deviation of the training dataset.

Training was conducted on a graphics processing unit (a single 12 GB NVIDIA GeForce GTX Titan), and the code was written with Keras. The mean squared error was used as

the loss, and the Adam optimizer was utilized for fast and robust training performance [32]. To obtain generalizable results, Gaussian noise with a measured standard deviation was added to the input tensor during training. The imposition of the simulated noise takes a role of regularization [33], and using the exact value of the measured standard deviation circumvents heuristic selection of hyperparameters. The minibatch size was 360. In each epoch, the network was validated on the test dataset. The validation loss decreased and eventually converged to 6.42e-4, while the training loss converged to 6.17e-4. The performance of the trained network will be validated with experimental data in Section IV.

III. SENSOR STRUCTURE AND FABRICATION

To implement a robust and reliable tactile sensor, it is necessary to simultaneously improve the sensor structure and fabrication process. The structure of the sensor is determined by considering the sensor's performance, such as spatial resolution and sensitivity. We also propose a fabrication method for establishing a stable sensing domain on large and curved surface. In this section, the sensor structure is introduced, including the shape of the sensor, the electrode configuration, the wiring, and the piezoresistive structure. Then, the fabrication process is explained step by step.

A. Sensor structure

An ERT-based tactile sensor can estimate external stimuli with only a few electrodes, but the sensor's performance varies with the placement of the electrodes. If the sensing region is far from the electrodes, the performance of the sensor will degrade due to the low current density, which is directly related to the sensitivity and spatial resolution. For example, the center region of the sensor will show poor spatial resolution and sensitivity when electrodes are placed only on the boundary [9]. Therefore, we attempt to evenly distribute the electrodes throughout the sensing domain. The conductive domain is formed on a cylindrical surface, and the electrodes are placed to form a triangular grid, as shown in **Fig. 3.** As shown in this figure, yellow dashed lines indicate the virtual triangular grid, and the electrodes are placed at the nodes of the grid.

A corresponding mesh model was also built for simulations. The length and diameter of the cylinder are 300 mm and 100 mm, respectively. The total number of electrodes is 30, and they are divided into 6 groups of 5 electrodes each. The electrodes in each group are placed on the same cross section of the cylinder at equal angular intervals. The distance between each electrode group is 60 mm. Wires are connected to the electrodes underneath the surface, and the electrodes are connected to the ERT multiplexer board through the wires.

The sensing domain needs to be not only conductive but also piezoresistive. Tawil et al. showed that a piezoresistive structure can be achieved by means of a contact-based transducing mechanism with conductive fabric [34]. When highly conductive fabric patches are attached to and pressed against the base conductive domain, a contact resistance appears, and current flows through the fabric patches, causing the sheet resistance to locally decrease. Similarly, we form a conductive surface on the rigid body of the skin and cover it
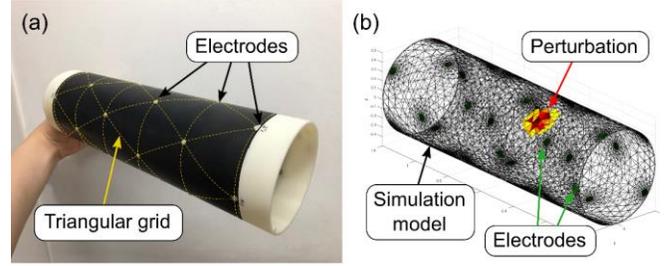

Figure 3. (a) Electrode configuration of the developed sensor (yellow: triangular grid); (b) corresponding simulation model (green: electrodes, red: simulated perturbation)
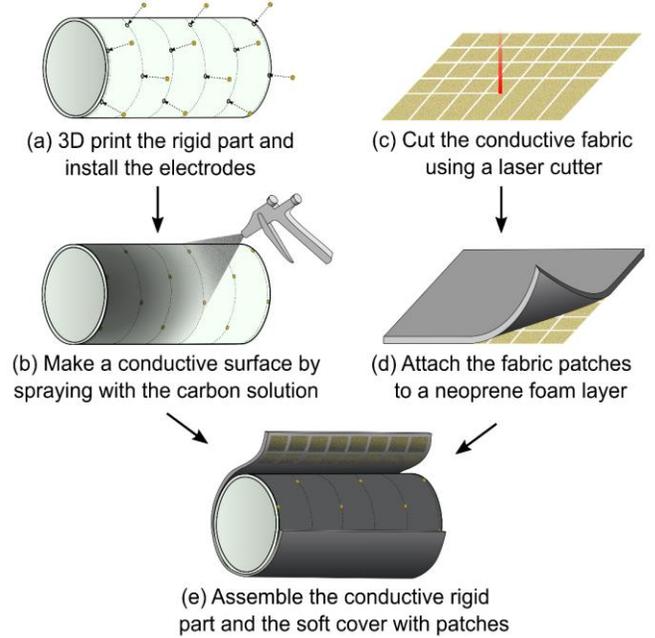

Figure 4. Sensor fabrication process: (a) base part with electrodes; (b) spray coating; (c) highly conductive fabric array; (d) attachment to neoprene foam; (e) assembly of the two parts

with a highly conductive layer to achieve piezoresistive characteristics.

B. Fabrication

The developed robotic skin consists of two parts: a conductive-coated rigid body with multiple embedded electrodes and a soft cover layer with highly conductive fabric patches. The overall fabrication process is shown in **Fig. 4**. The rigid base part was printed with a 3D printer (Dimension Elite, Stratasys, USA) and finished with an epoxy (XTC-3D, Smooth-On, USA). The part was also sanded to achieve fine surface conditions. The electrodes were installed on the rigid body and connected to the connector with electrical wires. To form the conductive surface, a CNT-dispersed solution (HANOS, Hanwha, South Korea) was sprayed several times until a suitable sheet resistance was achieved. Silver paste (ELCOAT P-100, CANS, Japan) was applied to the electrodes to establish a stable electrical connection between the coating surface and the electrodes. The base part was completed once the silver paste had dried sufficiently.

The soft cover layer was fabricated with a stretchable polyurethane (PU) film (Stretchfix, Vlieseline, Germany) and
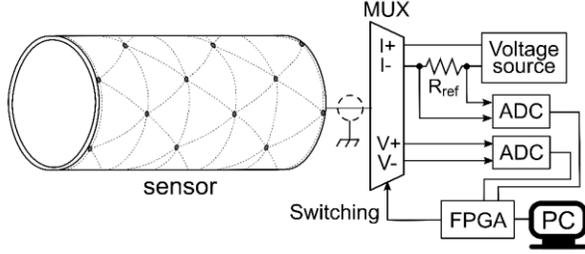
Figure 5. Schematic of the operating system of the ERT sensor

a highly conductive fabric (Med-tex P130, Statex, Germany). The PU film was applied to the fabric by ironing. The fabric was placed on a laser cutter and cut into an array of patches. Neoprene foam was then placed on the array of patches and fixed with glue.

Finally, the rigid part of the sensor was covered with the soft cover layer. The completed sensor exhibits piezoresistive characteristics due to the contact resistance between the CNT coating layer and the highly conductive fabric patches.

C. Electronics of the ERT system

To use an ERT-based sensor, it is necessary to perform current injection and measurement on the electrodes. For efficient implementation, we have chosen to use a pairwise injection and measurement scheme [35]. The electrodes are connected to a multiplexer (ADG1206, Analog Devices, USA), which is controlled by a DAQ (myRIO-1900, National Instruments, USA). The multiplexer is also connected to a current source and a voltage measurement channel to enable current injection and voltage measurement on the electrodes. The schematic of the ERT operating system is shown in **Fig. 5**. Instead of using a constant current source, we use a constant voltage source and a serially connected reference resistor for compensation. In addition, the DAQ has an FPGA chip, enabling switching and measurement up to 120 kHz. Due to the fast sampling rate, the developed sensor also has a high frame rate of 120 Hz.

IV. EXPERIMENTS AND RESULTS

A. Indentation experiment setup

We conducted an indentation experiment with the setup shown in **Fig. 6**. The sensor was fixed to a shaft and connected to a stepper motor. The indenter consisted of a voice coil (VC) motor, a load cell, and a spherical tip. The indenter was installed on a linear motion guide and connected to another stepper motor via a timing belt to allow it to move along the linear guide. During the experiment, we indented the sensor 900 times at the nodes of a 30x30 rectangular grid. When the indenter had moved to the proper position, the sensor was indented, and the sensor output, position, and force value were logged simultaneously. Then, these single-point indentation data were used to evaluate the sensor performance, such as its localization accuracy, distribution of spatial sensitivity, and imaging clarity.

B. Localization performance

The experimental data were converted into a conductivity image (30x30) by using a regularization method (linear) and the DNN-based method, and the centroids of the reconstructed image (x_m, y_m) were calculated from the
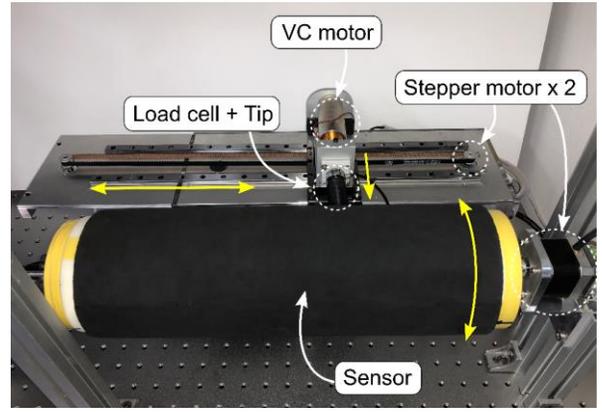

Figure 6. Indentation experiment setup, including an indenter (VC motor, load cell, and tip) and a moving stage for the indenter
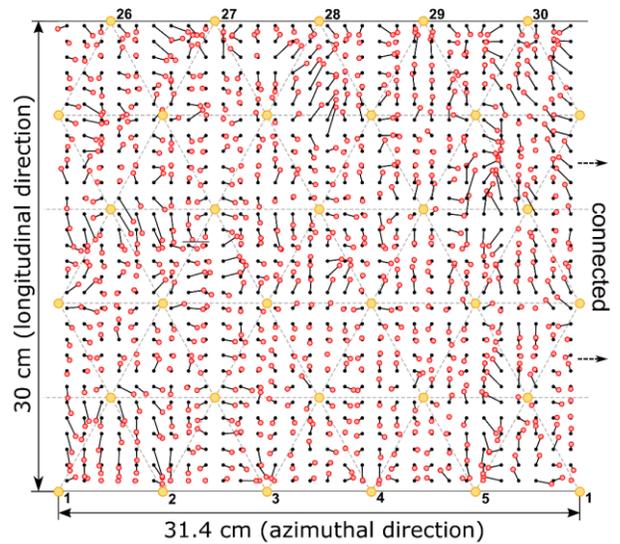

Figure 7. Localization result with DNN-based reconstruction

output image:

$$(x_m, y_{m)} = \left(\frac{\sum m_i x_i}{\sum m_i}, \frac{\sum m_i y_i}{\sum m_i} \right) \tag{11}$$

where $i = 1, \dots, 900$. Then, the positions of the centroids were compared with the indentation locations. The localization errors of the DNN-based method and the regularization method were 5.2 ± 3.3 mm and 5.5 ± 3.2 mm, respectively. These results indicate that the localization performance of the sensor is significantly improved compared to that achieved in the previous study [9]. In addition, the estimated centroids are not biased toward the center of the sensor because of the connectivity of the conductive domain. The DNN-based localization result is shown in **Fig. 7**. Note that the left and right edges of the plot are connected on the cylindrical surface. The black dots and red circles indicate the indentation locations and the corresponding estimates, respectively. The yellow circles indicate the positions of the electrodes.

C. Sensitivity fluctuation

The scale of the resulting voltage change is determined by the current density at the indentation location. Since the
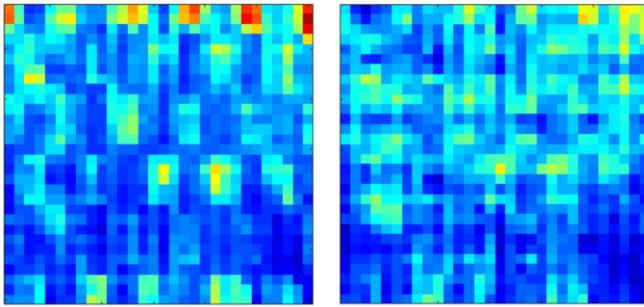
Figure 8. Sensitivity distributions of the developed sensor:
(a) regularization method; (b) DNN-based method

Figure 9. Reconstructed conductivity images:
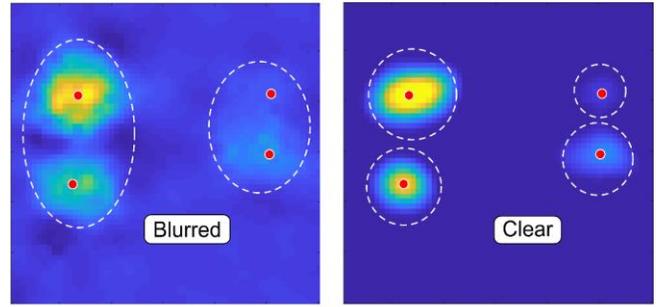**(a) regularization method; (b) DNN-based method**

current density varies with the location and drive pattern, the sensitivity of the sensor also fluctuates. We attempt to solve this problem by using a DNN, and we compare the results with those of the regularization method. For an output image $I_{i,j}$ obtained from the output voltages observed with an indentation at position (i, j), the sensitivity distribution $C_{i,j}$ is calculated by dividing the peak value of the reconstructed image $I_{i,j}$ by the corresponding measured force value $F_{i,j}$:

$$C_{i,j} = \frac{\max(I_{i,j})}{F_{i,j}} \tag{12}$$

where $i = 1, \ldots, 30$ and $j = 1, \ldots, 30$. The corresponding sensitivity distributions are shown in **Fig. 8**. When the standard deviations of the sensitivity distributions are normalized with respect to the average sensitivity value, the corresponding standard distributions are 0.39 and 0.45 for the DNN-based method and the regularization method, respectively. These findings indicate that the sensitivity distribution of the sensor becomes more uniform with DNN-based reconstruction.

D. Image reconstruction results

We have used the data from the previously described indentation experiment to quantitatively evaluate the sensor performance, but this experiment considered only single-point indentation. If the sensor is indented at multiple locations simultaneously, the reconstructed image becomes blurred and distorted because of the nonlinear characteristics of the sensor. To provide an example, we simultaneously indented four locations on the sensor by hand to obtain the corresponding measurement data and then converted these data into heatmap images, as shown in **Fig. 9**. The red dots indicate the indentation locations. Images (a) and (b) were reconstructed using the linear method (regularization) and the DNN-based method, respectively. The results show that the linear method yields a blurred and noisy image, in which it is not easy to distinguish each indentation location. In contrast, the DNN-based method produces a sharper image, in which each perturbation can be clearly distinguished. This is because the neural network can partially compensate for the nonlinear behavior of the sensor. These results also qualitatively imply that the DNN-based method can improve the spatial resolution (two-point discriminability) of the sensor.

V. DISCUSSION AND CONCLUSION

This paper has introduced an ERT-based robotic skin with sparsely distributed electrodes, including the design, fabrication, and DNN-based signal processing (image reconstruction) of the proposed system. The electrodes are used for injecting current and measuring the resulting voltages, and they are sparsely distributed and firmly embedded in the developed sensor. Since the wires are not directly exposed to the outside, the developed robotic skin is robust and clean. The base conductive domain is formed by spraying a CNT-dispersed solution; consequently, a conductive domain can be formed on any curved surface. Highly conductive fabric patches are also applied to establish a piezoresistive structure in the sensing domain. Due to the simple, durable, and customizable sensor structure, it would be possible to integrate the proposed tactile sensing method into a commercialized robot arm.

To evaluate the performance of the sensor and the neural network, we conducted an indentation experiment using a rotary indenter setup. The localization errors of the DNN-based method and the regularization method were 5.2 ± 3.3 mm and 5.5 ± 3.2 mm, respectively. Considering the number of electrodes (N=30) and the size of the sensing domain (30 cm x 31.4 cm), these results are remarkable. This result could be improved by increasing the number of electrodes. However, the localization accuracy of the DNN-based method and the regularization method (linear) are very similar because the linear reconstruction matrix was derived by regularizing the Jacobian matrix obtained from a simulation with single-element perturbations.

The sensitivity of the sensor was also quantified based on the measured force and peak value corresponding to each recorded image, and the results revealed that the sensitivity fluctuations are partially mitigated by the DNN. This demonstrates that the proposed ERT-based tactile sensor can be calibrated using a DNN and measurement data. In addition, we compared the quality of the reconstructed images for a case of multipoint indentation. Even two stimuli in close proximity were clearly distinguishable with the DNN-based method because the DNN can compensate for the nonlinear behavior of the sensor. Consequently, the spatial resolution of the sensor is improved by the DNN-based method.

REFERENCES

[1] S. Haddadin *et al.*, "On making robots understand safety: Embedding injury knowledge into control," *Int. J. Rob. Res.*, vol. 31, no. 13, pp. 1578–1602, 2012.

[2] C. Paxton, Y. Barnoy, K. Katyal, R. Arora, and G. D. Hager, "Visual Robot Task Planning," pp. 8832–8838, 2018.

[3] M. A. Lee *et al.*, "Making Sense of Vision and Touch : Self-Supervised Learning of Multimodal Representations for Contact-Rich Tasks," pp. 8943–8950, 2019.

[4] K. Park, S. Kim, H. Lee, I. Park, and J. Kim, "Low-hysteresis and low-interference soft tactile sensor using a conductive coated porous elastomer and a structure for interference reduction," *Sensors Actuators, A Phys.*, vol. 295, pp. 541–550, 2019.

[5] A. Schmitz, P. Maiolino, M. Maggiali, L. Natale, G. Cannata, and G. Metta, "Methods and technologies for the implementation of large-scale robot tactile sensors," *IEEE Trans. Robot.*, vol. 27, no. 3, pp. 389–400, 2011.

[6] G. Cannata, M. Maggiali, G. Metta, and G. Sandini, "An embedded artificial skin for humanoid robots," *IEEE Int. Conf. Multisens. Fusion Integr. Intell. Syst.*, pp. 434–438, 2008.

[7] P. Mittendorfer and G. Cheng, "Humanoid multimodal tactile-sensing modules," *IEEE Trans. Robot.*, vol. 27, no. 3, pp. 401–410, 2011.

[8] D. Silvera-Tawil, D. Rye, M. Soleimani, and M. Velonaki, "Electrical impedance tomography for artificial sensitive robotic skin: A review," *IEEE Sens. J.*, vol. 15, no. 4, pp. 2001–2016, 2015.

[9] H. Lee *et al.*, "Internal Array Electrodes Improve the Spatial Resolution of Soft Tactile Sensors Based on Electrical Resistance Tomography," *2019 IEEE Int. Conf. Robot. Autom.*, pp. 5411–5417, 2019.

[10] T. Rymarczyk, "Application of neural reconstruction of tomographic images in the problem of reliability of flood protection facilities Zastosowanie neuronowej rekonstrukcji obrazów tomograficznych w problematyce niezawodności zabezpie," vol. 20, no. 3, pp. 425–434, 2018.

[11] G. Bouchette, P. Church, J. E. McFee, and A. Adler, "Imaging of compact objects buried in underwater sediments using electrical impedance tomography," *IEEE Trans. Geosci. Remote Sens.*, vol. 52, no. 2, pp. 1407–1417, 2014.

[12] P. Church, J. E. McFee, S. Gagnon, and P. Wort, "Electrical impedance tomographic imaging of buried landmines," *IEEE Trans. Geosci. Remote Sens.*, vol. 44, no. 9, pp. 2407–2420, 2006.

[13] E. Zimmermann, A. Kemna, J. Berwix, W. Glaas, and H. Vereecken, "EIT measurement system with high phase accuracy for the imaging of spectral induced polarization properties of soils and sediments," *Meas. Sci. Technol.*, vol. 19, no. 9, 2008.

[14] A. Borsic, B. M. Graham, A. Adler, and W. R. B. Lionheart, "In Vivo Impedance Imaging With Total Variation Regularization," *IEEE Trans. Med. Imaging*, vol. 29, no. 1, pp. 44–54, 2010.

[15] R. J. Halter, A. Hartov, and K. D. Paulsen, "A broadband high-frequency electrical impedance tomography system for breast imaging," *IEEE Trans. Biomed. Eng.*, vol. 55, no. 2, pp. 650–659, 2008.

[16] M. T. Clay and T. C. Ferree, "Weighted regularization in electrical impedance tomography with applications to acute cerebral stroke," *IEEE Trans. Med. Imaging*, vol. 21, no. 6, pp. 629–638, 2002.

[17] T. Tidswell, A. Gibson, R. H. Bayford, and D. S. Holder, "Three-dimensional electrical impedance tomography of human brain activity," *Neuroimage*, vol. 13, no. 2, pp. 283–294, 2001.

[18] H. Garbaa, L. Jackowska-Strumiłło, K. Grudzień, and A. Romanowski, "Application of electrical capacitance tomography and artificial neural networks to rapid estimation of cylindrical shape parameters of industrial flow structure," *Arch. Electr. Eng.*, vol. 65, no. 4, pp. 657–669, 2016.

[19] J. Jia, M. Wang, H. I. Schlaberg, and H. Li, "A novel tomographic sensing system for high electrically conductive multiphase flow measurement," *Flow Meas. Instrum.*, vol. 21, no. 3, pp. 184–190, 2010.

[20] A. Seppänen, A. Voutilainen, and J. P. Kaipio, "State estimation in process tomography - Reconstruction of velocity fields using EIT," *Inverse Probl.*, vol. 25, no. 8, 2009.

[21] H. S. Tapp, A. J. Peyton, E. K. Kemsley, and R. H. Wilson, "Chemical engineering applications of electrical process tomography," *Sensors Actuators, B Chem.*, vol. 92, no. 1–2, pp. 17–24, 2003.

[22] M. Vauhkonen, W. R. Lionheart, L. M. Heikkinen, P. J. Vauhkonen, and J. P. Kaipio, "A MATLAB package for the EIDORS project to reconstruct two-dimensional EIT images.," *Physiol. Meas.*, vol. 22, no. 1, pp. 107–111, 2001.

[23] A. Adler and W. R. B. Lionheart, "EIDORS: Towards a community-based extensible software base for EIT," *6th Conf. Biomed. Appl. Electr. Impedance Tomogr. London, UK*, pp. 1–4, 2005.

[24] W. R. B. Lionheart, K. Paridis, and A. Adler, "Resistor networks and transfer resistance matrices," in *13th International Conference on Biomedical Applications of Electrical Impedance Tomography*, 2012, pp. 23–25.

[25] D. Isaacson, S. Simske, J. Goble, J. C. Newell, and M. Cheney, "NOSER: An algorithm for solving the inverse conductivity problem," *Int. J. Imaging Syst. Technol.*, vol. 2, no. 2, pp. 66–75, 1990.

[26] S. Liu, J. Jia, Y. D. Zhang, and Y. Yang, "Image Reconstruction in Electrical Impedance Tomography Based on Structure-Aware Sparse Bayesian Learning," *IEEE Trans. Med. Imaging*, vol. 37, no. 9, pp. 2090–2102, 2018.

[27]   M. Michalikova, M. Prauzek, and J. Koziorek, "Impact of the Radial basis function spread factor onto image reconstruction in electrical impedance tomography," *IFAC-PapersOnLine*, vol. 28, no. 4, pp. 230–233, 2015.

[28]   P. C. Shetiye, "Detection of Breast Cancer Using Electrical Impedance and RBF Neural Network," *Int. J. Inf. Electron. Eng.*, vol. 5, no. 5, 2015.

[29]   A. Adler and R. Guardo, "A Neural Network Image Reconstruction Technique for Electrical Impedance Tomography," *IEEE Trans. Med. Imaging*, vol. 13, no. 4, pp. 594–600, 1994.

[30]   S. Russo and R. Assaf, "Towards a practical Implementation of EIT-based Sensors using Artificial Neural Networks," pp. 9–11, 2017.

[31]   H. Park *et al.*, "Deep Neural Network Approach in Electrical Impedance Tomography-based Real-time Soft Tactile Sensor," pp. 7441–7446, 2019.

[32]   D. P. Kingma and J. Lei Ba, "ADAM: A METHOD FOR STOCHASTIC OPTIMIZATION," in *Iclr*, 2015, pp. 1–15.

[33]   C. M. Bishop, "Training with Noise is Equivalent to Tikhonov Regularization," *Neural Comput.*, vol. 7, no. 1, pp. 108–116, 1995.

[34]   D. S. Tawil, D. Rye, and M. Velonaki, "Improved image reconstruction for an EIT-based sensitive skin with multiple internal electrodes," *IEEE Trans. Robot.*, vol. 27, no. 3, pp. 425–435, 2011.

[35]   D. S. Holder and A. J. Temple, "Effectiveness of the Sheffield EIT system in distinguishing patients with pulmonary pathology from a series of normal subjects," *Clin. Physiol. Appl. Electr. impedance Tomogr.*, pp. 277–298, 1993.